Nucleic Acids Research, 2016, Vol. 44, No. 8 **3829–3844**
doi: 10.1093/nar/gkw228

Reversal of DNA damage induced Topoisomerase 2 DNA–protein crosslinks by Tdp2

Matthew J. Schellenberg[1], Lalith Perera[1], Christina N. Strom[2], Crystal A. Waters[2], Brinda Monian[1], C. Denise Appel[1], Caroline K. Vilas[1], Jason G. Williams[3], Dale A. Ramsden[2] and R. Scott Williams[1,*]

[1]Genome Integrity and Structural Biology Laboratory, National Institute of Environmental Health Sciences, US National Institutes of Health, Department of Health and Human Services, Research Triangle Park, NC 27709, USA, [2]Lineberger Comprehensive Cancer, University of North Carolina at Chapel Hill, Chapel Hill, NC 27599, USA and [3]Epigenetics and Stem Cell Biology Laboratory, National Institute of Environmental Health Sciences, US National Institutes of Health, Department of Health and Human Services, Research Triangle Park, NC 27709, USA

Received February 09, 2016; Revised March 22, 2016; Accepted March 23, 2016

ABSTRACT

Mammalian Tyrosyl-DNA phosphodiesterase 2 (Tdp2) reverses Topoisomerase 2 (Top2) DNA–protein crosslinks triggered by Top2 engagement of DNA damage or poisoning by anticancer drugs. Tdp2 deficiencies are linked to neurological disease and cellular sensitivity to Top2 poisons. Herein, we report X-ray crystal structures of ligand-free Tdp2 and Tdp2-DNA complexes with alkylated and abasic DNA that unveil a dynamic Tdp2 active site lid and deep substrate binding trench well-suited for engaging the diverse DNA damage triggers of abortive Top2 reactions. Modeling of a proposed Tdp2 reaction coordinate, combined with mutagenesis and biochemical studies support a single Mg^{2+}-ion mechanism assisted by a phosphotyrosyl-arginine cation-π interface. We further identify a Tdp2 active site SNP that ablates Tdp2 Mg^{2+} binding and catalytic activity, impairs Tdp2 mediated NHEJ of tyrosine blocked termini, and renders cells sensitive to the anticancer agent etoposide. Collectively, our results provide a structural mechanism for Tdp2 engagement of heterogeneous DNA damage that causes Top2 poisoning, and indicate that evaluation of Tdp2 status may be an important personalized medicine biomarker informing on individual sensitivities to chemotherapeutic Top2 poisons.

INTRODUCTION

Nuclear DNA compaction and the action of DNA and RNA polymerases create positive and negative DNA supercoiling—over- and under-winding of DNA strands, respectively—and the linking together (catenation) of DNA strands. Topoisomerases relieve topological DNA strain and entanglement to facilitate critical nuclear DNA transactions including DNA replication, transcription and cell division. The mammalian type II topoisomerases Top2α and Top2β enzymes generate transient, reversible DNA double strand breaks (DSBs) to drive topological transactions (1–3). Reversibility of Top2 DNA cleavage reactions is facilitated by formation of covalent enzyme phosphotyrosyl linkages between the 5′-phosphate ends of the incised duplex and an active site Top2 tyrosine, resulting in Top2 cleavage complexes (Top2cc).

The Top2cc protein–DNA adduct is a unique threat to genomic integrity which must be resolved to prevent catastrophic Top2cc collisions with the cellular replication and transcription machineries (4–7). To promote cancer cell death, Top2 reactions are ‘poisoned’ by keystone pharmacological anticancer agents like etoposide, teniposide and doxorubicin. Importantly, Top2 is also poisoned when it engages abundant endogenous DNA damage not limited to but including ribonucleotides (8,9), abasic sites (10–14) and alkylation damage such as exocyclic DNA adducts arising from bioactivation of the vinyl chloride carcinogen (15,16) (Figure 1A). In the case of DNA damage-triggered Top2cc, compound DNA lesions arise that consist of the instigating lesion, and a DNA DSB bearing a bulky terminal 5′-linked Top2 DNA–protein crosslink. The chemical complexity of DNA damage-derived Top2cc necessitates that DNA repair machinery dedicated to resolving these lesions recognizes both DNA and protein, whilst accommodating diverse chemical structures that trap Top2cc. Precisely how the cellular DNA repair machinery navigates these complex lesions is an important aspect of Top2cc repair that has not yet been explored.

Tyrosyl DNA phosphodiesterase 2 (Tdp2) directly hydrolyzes 5′-phosphotyrosyl (5′-Y) linkages, and is a key

---

[*] To whom correspondence should be addressed. Tel: +1 919 541 4652; Fax: +1 301 480 3583; Email: williamsrs@niehs.nih.gov

Published by Oxford University Press on behalf of Nucleic Acids Research 2016.

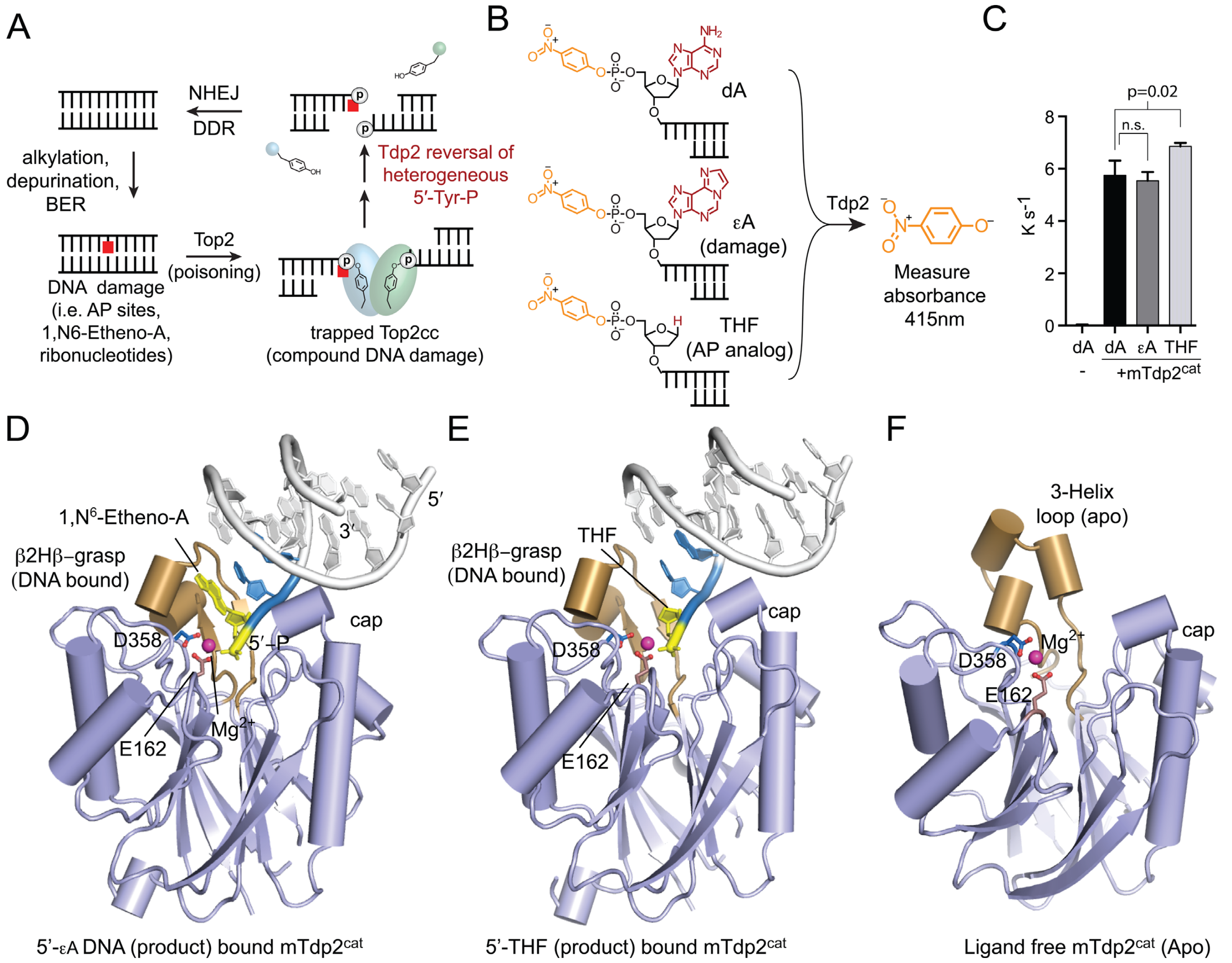

Figure 1. Tdp2 processes phosphotyrosyl linkages in diverse DNA damage contexts. (**A**) Unrepaired DNA damage and repair intermediates such as bulky DNA adducts, ribonucleotides or abasic sites can poison Top2 and trap Top2 cleavage complex (Top2cc), resulting in a DSB with a 5′–Top2 protein adduct linked by a phosphotyrosine bond. Tdp2 hydrolyzes the 5′–phosphotyrosine adduct derived from poisoned Top2 leaving DNA ends with a 5′-phosphate, which facilitates DNA end joining through the NHEJ pathway. (**B**) DNA oligonucleotide substrates synthesized by EDC-imidazole coupling and used in Tdp2 enzyme assays contain deoxyadenine (dA), Ethenoadenine (εA) or an abasic site (THF) and a 5′–nitrophenol moiety. Phosphotyrosyl bond hydrolysis catalyzed by mTdp2^{cat} releases *p*-nitrophenol, which is detected by measuring absorbance at 415 nm. (**C**) mTdp2^{cat} reaction rates on *p*–nitrophenol modified DNA substrates shown in panel B. Rates are reported as molecules of PNP s^{-1} produced by mTdp2^{cat}. *P*-values calculated using two-tailed t-test; error bars, s.d. n = 4, n.s. = not statistically significant. (**D**) Structure of mTdp2^{cat} bound to 5′-phosphate DNA (product complex) containing εA (yellow). DNA binding β2Hβ–grasp (tan) and cap elements engage the 5′-nucleotide as well as the +2 and +3 nucleotides (blue) of substrate DNA. PDB entry 5HT2 is displayed, also see Table 1. (**E**) Structure of mTdp2^{cat} bound to 5′-phosphate DNA (product complex) containing THF (yellow). DNA binding β2Hβ–grasp (tan) and cap elements engage the 5′-nucleotide as well as the +2 and +3 nucleotides (blue) of substrate DNA. PDB entry 5INK is displayed, also see Table 1. (**F**) Structure of mTdp2^{cat} in the absence of DNA showing the extended 3-helix loop (tan) open-conformation of the DNA-binding grasp as seen in monomer E of the apo structure. PDB entry 5INM is displayed, also see Table 1.

modulator of cellular resistance to chemotherapeutic Top2 poisons (17–20). Tdp2 knockdown sensitizes A549 lung cancer cells to etoposide, and increases formation of nuclear γH2AX foci, a marker of DSBs (17), underlining the importance of Tdp2 in cellular Top2cc repair. Tdp2 is overexpressed in lung cancers, is transcriptionally up-regulated in mutant p53 cells and mediates mutant p53 gain of function phenotypes, which can lead to acquisition of therapy resistance during cancer progression (21). The importance of Tdp2 in mediating topoisomerase biology is further underlined by the facts that human *TDP2* inactivating mutations are found in individuals with intellectual disabilities, seizures and ataxia, and at the cellular level, loss of Tdp2 inhibits Top2β-dependent transcription (18). It is possible that *TDP2* single nucleotide polymorphisms (SNPs) encode mutations that impact Tdp2 function, but the molecular underpinnings for such Tdp2 deficiencies are not understood.

Previously we reported high-resolution X-ray crystal structures of the minimal catalytically active endonuclease/exonuclease/phosphatase (EEP) domain of mouse Tdp2 (mTdp2^{cat}) bound to a DNA substrate mimic, and a 5′-phosphorylated reaction product (20). However, important questions regarding the mechanism of Tdp2 engagement and processing of DNA damage remain. First, it is unclear if Tdp2 processes phosphotyrosyl linkages in the context of DNA damage that triggers Top2cc, and if so, how the enzyme can accommodate such complex DNA damage within its active site. Based on metal-bound Tdp2 structures (20), we also proposed a single Mg^{2+} mediated catalytic mechanism, but this mechanism requires further scrutiny and characterization. Herein, we report an integrated structure-function study of the Tdp2 reaction mechanism, including a description of new X-ray structures of ligand-free Tdp2, and Tdp2 bound to abasic and alkylated (1-N^6-etheno-adenine) DNA damage. Our integrated results from structural analysis, mutagenesis, functional assays and quanyum mechanics/molecular mechanics (QM/MM) modeling of the Tdp2 reaction coordinate describe in detail how Tdp2 mediates a single-metal ion tyrosyl DNA phosphodiesterase reaction capable of acting on diverse DNA end damage. We further establish that DNA damage binding in the Tdp2 active site is linked to conformational change and binding of metal cofactor. Finally, we characterize a Tdp2 SNP that ablates the Tdp2 single metal binding site and Tdp2 substrate induced conformational changes, and confers Top2 drug sensitivity in mammalian cells.

MATERIALS AND METHODS

Generation of PNP modified oligonucleotide substrates

Oligonucleotides with a 5′-phosphate modification were obtained from IDT and diluted to a concentration of 2 mmol l^{-1} in water. 1-Ethyl-3-(3-dimethylaminopropyl) carbodiimide (EDC; Pierce) was used to couple *p*-nitrophenol to the oligonucleotide with a modified version of the manufacturer's instructions. Briefly, 25 mg EDC were dissolved in 150 μl oligonucleotide solution. After the EDC dissolved, 400 μl DDW, 60 μl 100 mmol l^{-1} Imidazole pH 6 and 100 μl of PNP from a saturated water/PNP mixture preheated to 55°C were added. Reactions were heated at 55°C for 30 min to ensure the PNP dissolved, then incubated at 37°C overnight. Reactions were quenched with 500 μl 2 mol l^{-1} acetic acid and heated to 55°C for 1 h, followed by neutralization with 500 μl 2 mol l^{-1} Tris base. Reactions were twice diluted to 15 ml in DDW then concentrated to 300 μl with a 3K MWT cutoff spin concentrator (Amicon), then run on 20% (w/v) 19:1 8M urea-TBE PAGE to resolve reaction products. Bands were visualized by UV shadow, excised, soaked in 15 ml DDW for 16 h at 15°C, and purified on a C18 reverse-phase Sep-Pac (Waters).

Protein expression, purification and crystallization

Mouse Tdp2 catalytic domain ($mTdp2^{cat}$, residues 118 to 370), human Tdp2 catalytic domain ($hTdp2^{cat}$, residues 108–362) or full-length human Tdp2 ($hTdp2^{FL}$, residues 1–362) were expressed and purified as previously described (20). Plasmids containing mutant Tdp2 sequences were generated using the Quickchange kit (Stratagene). Crystals containing $mTdp2^{cat}$ and 5′-phosphorylated DNA (product) with modified 5′ nucleotides (ϵA, dA, THF) were grown and cryoprotected as described (20). Sequences, modifications and synthesis sources for oligonucleotides used for co-crystallization are indicated in Supplementary Table S1. For alternate divalent metal complexes, a 5′-phosphorylated DNA substrate (substrate dC) was co-crystallized in the presence of Mg^{2+}, and divalent metals were swapped by soaking the crystals in crystallization buffer containing 5 mmol l^{-1} $MnCl_2$ or 10 mmol l^{-1} $Ca(OAc)_2$ for 1 h prior to cryoprotection. Cryoprotectant solutions contained mother liquor plus 25% PEG-3350, 8% glycerol and 5% glucose, and either 5 mmol l^{-1} $MnCl_2$ or 10 mmol l^{-1} $Ca(OAc)_2$.

Crystals of $hTdp2^{cat}$ bound to 5′-phosphate DNA (substrate dC) were prepared by mixing a 1.2-fold molar excess of DNA, and grown in 90 mmol l^{-1} TRIS pH 7.0, 27% (w/v) PEG600, 9% (v/v) glycerol and 450 mmol l^{-1} $(NH_4)_2SO_4$. Crystals of apo-$mTdp2^{cat}$ were grown in 14–18% (w/v) PEG3350, 100 mmol l^{-1} HEPES pH 7.5, 200 mmol l^{-1} Li_2SO_4 and 10 mmol l^{-1} $Mg(OAc)_2$, and soaked into the same buffer containing 25% PEG3350 and 12% (v/v) glycerol prior to flash-freezing in liquid nitrogen for data collection.

X-ray diffraction data collection, phasing and refinement

X-ray data (Table 1) for all structures except the manganese soak (PDB entry 5INP) were collected at 100 K on beamline 22-ID of the Advanced Photon Source at a wavelength of 1.000 Å. X-ray data for the manganese soak (PDB entry 5INP) were collected on a Rigaku HF007 Cu rotating anode X-ray source at a wavelength of 1.5418 Å. X-ray diffraction data were processed and scaled using the HKL2000 suite (22). The $hTdp2^{cat}$-DNA and $mTdp2^{cat}$-apo crystals were phased by molecular replacement in PHASER (23) using chain A of PDB entry 4GZ1. Initial solutions were improved by iterative rounds of manual fitting in COOT (24) and refinement in PHENIX (25).

Limited proteolysis assays

For proteolysis experiments, 4 μl reactions containing 40 μmol l^{-1} $mTdp2^{cat}$ (aa 118 to 370) in reaction buffer (10 mmol l^{-1} HEPES pH 7.5, 200 mmol l^{-1} NaCl, 0.5 mmol L^{-1} TCEP) with 4 mmol l^{-1} $Mg(OAc)_2$ (indicated +Mg) or 8 mmol l^{-1} NaOAc (indicated -Mg), with 0 or 60 μmol l^{-1} 12 nt DNA were incubated with 0, 5, 1.7 or 0.6 μg l^{-1} Trypsin for 1 h at 22°C. Reactions were quenched by addition of Laemmli SDS-PAGE dye, heated at 70°C for 10 min, and analyzed by SDS-PAGE. For mass-spectrometry analysis of peptide masses, reactions were quenched with 1% (v/v) trifluoroacetic acid , purified on a C18 ZipTip (Millipore) and an ESI-MS mass measurement made on a Q-ToF Ultima/Global (Micromass/Waters) using flow injection from a pressurized bomb. The instrument was operated in the positive ion, V-mode and calibrated using the multiply-charged ion envelope of horse heart cytochrome C. The molecular ion mass was determined using the Max Ent 1 routine from the MassLynx software.

Intrinsic tryptophan fluorescence

Reactions contained 50 μl with 1 μmol l^{-1} $mTdp2^{cat}$ (residues 118 to 370) in buffer (6 mmol l^{-1} HEPES pH

Table 1. Data collection and refinement statistics

PDB entry ID	mTdp2 118–370 5′-P +ϵA 5HT2	mTdp2 118–370 5′-P + THF 5INK	mTdp2 118–370 5′-P + dA 5INL	mTdp2 118–370 wt, apo 5INM	mTdp2 118–370 D358N, apo 5INN	hTdp2 108–362 5′-P DNA 5INO	mTdp2 118–370 5′-P DNA Mn^{2+} soak 5INP	mTdp2 118–370 5′-P DNA Ca^{2+} soak 5INQ
Data collection								
Space group	$P\,2_1\,2_1\,2_1$	$P\,2_1\,2_1\,2_1$	$P\,2_1\,2_1\,2_1$	$P\,2_1\,2_1\,2_1$	$P\,2_1\,2_1\,2_1$	$P\,3_1$	$P\,2_1\,2_1\,2_1$	$P\,2_1\,2_1\,2_1$
Cell dimensions								
a, b, c (Å)	54.88, 68.60, 167.25	54.62, 67.66, 166.74	54.90, 69.05, 167.80	95.85, 113.44, 114.96	95.44, 114.88, 115.45	69.66, 69.66, 120.68	54.92, 68.52, 166.90	54.70, 67.50, 167.52
α, β, γ (°)	90, 90, 90	90, 90, 90	90, 90, 90	90, 90, 90	90, 90, 90	90, 90, 120	90, 90, 90	90, 90, 90
Resolution (Å)	50–1.43 (1.48–1.43)	50–2.15 (2.23–2.15)	50–1.55 (1.61–1.55)	50–2.40 (2.49–2.40)	50–2.80 (2.90–2.80)	50–3.20 (3.31–3.20)	50–1.95 (2.02–1.95)	50–1.85 (1.92–1.85)
R_{sym} or R_{merge}	0.051 (0.599)	0.125 (0.650)	0.067 (0.588)	0.124 (0.518)	0.113 (0.459)	0.082 (0.574)	0.054 (0.181)	0.068 (0.564)
$I / \sigma I$	21.0 (2.1)	17.5 (2.7)	19.4 (2.4)	9.8 (2.1)	10.6 (2.0)	15.5 (2.2)	25.5 (4.8)	21.1 (3.1)
Completeness (%)	97.4 (86.6)	98.4 (95.4)	99.0 (91.5)	98.0 (94.2)	95.7 (93.0)	100 (100)	97.1 (80.7)	99.9 (100)
Redundancy	3.9 (3.0)	6.7 (6.5)	5.4 (3.7)	4.2 (3.6)	4.2 (3.4)	3.9 (3.9)	5.5 (2.0)	6.0 (6.0)
Refinement								
Resolution (Å)	29.9–1.43	45.7–2.15	34.1–1.55	48.8–2.4	49.3–2.80	34.8–3.205	29.8–1.95	39.1–1.85
No. reflections	114 115	34 369	91 871	49 905	29 807	10 757	45 238	53 889
R_{work} / R_{free}	0.116/0.150	0.167/0.201	0.129/0.168	0.183/0.233	0.214/0.255	0.214/0.264	0.152/0.179	0.164/0.200
Non-H atoms								
Protein/DNA	4552	4372	4600	9621	9411	4363	4512	4452
Ligand/ion	25	22	25	25	28	5	15	21
Water	726	449	721	365	148	5	444	374
B-factors (Å^2)								
Protein/DNA	26.5	35.8	26.7	47.7	53.3	147.9	35.6	50.4
Ligand/ion	52.5	50.2	53.0	73.5	82.2	225.8	53.7	54.7
Water	44.2	43.0	46.0	38.2	28.3	83.3	44.7	52.4
R.m.s. deviations								
Bond lengths (Å)	0.007	0.007	0.005	0.004	0.002	0.003	0.007	0.008
Bond angles (°)	1.18	1.01	0.85	0.81	0.58	0.78	1.03	1.08

Each data set was collected from a single crystal. Values in parentheses are for highest-resolution shell (10% of relections).

7.5, 300 mmol l^{-1} NaCl, 0.3 mmol L^{-1} TCEP and 0.01% (v/v) TWEEN-20) with 0–20 mmol l^{-1} $Mg(OAc)_2$ or ultrapure $Ca(OAc)_2$ (99.9965%, Alfa Aesar) titrated against 0–40 mmol l^{-1} NaOAc to maintain a constant concentration of acetate, with 0 or 1.5 μmol l^{-1} 12 nt DNA. Reactions were incubated at room temperature for 20 minutes in a 96-well black plastic plate (Corning), then tryptophan fluorescence was measured in a Polarstar Omega platereader (BMG Labtech) with 4 readings of 150 pulses per well using 280/10 excitation and 350/10 emission filters. The increase in fluorescent intensity was calculated by subtracting the fluorescent intensity from samples with no divalent metal ions and plotted as a function of divalent metal ion concentration. K_d values and Hill coefficients were calculated using PRISM6.

Tdp2 enzyme assays

Assays on MBP-fusion proteins of the human catalytic domain (MBP-hTdp2^{cat}) mutant proteins with 5′ -tyrosylated DNA substrates (Figures 5E and 6C and Supplementary Figure S5C) were performed as described (20). For experiments measuring the effect of divalent metal ions on reaction rates, 50 μl reactions contained 1 μmol l^{-1} mTdp2^{cat} (residues 118 to 370, Figure 4B), hTdp2^{cat} (residues 108–362) or hTdp2^{FL} (residues 108–362) in buffer (10 mmol l^{-1} HEPES pH 7.5, 100 mmol l^{-1} NaCl, 0.5 mmol l^{-1} TCEP, 0.4 mg ml^{-1} BSA, 0.02% (v/v) TWEEN-20, 1 mmol l^{-1} Thymidine 5′–*p*-nitrophenyl phosphate) with 0–100 mmol l^{-1} $Mg(OAc)_2$ titrated against 20–220 mmol l^{-1} NaOAc to maintain a constant concentration of acetate. Reactions contained 0, 1 or 10 mmol l^{-1} ultrapure $Ca(OAc)_2$ (99.9965%, Alfa Aesar), with 0, 2 or 20 mmol l^{-1} less NaOAc to maintain a constant acetate concentration. PNP formation was monitored by the absorbance at 415 nm with a background correction at 515 nm. The change in absorbance at 415 nm at 10 min as a function of Mg^{2+} concentration was plotted.

Preparation of NHEJ substrates

Oligonucleotide 300 bp substrates with 5′ phosphorylated GATC overhangs were generated as previously described (26). Comparable substrate with 5′-phophotyrosine adducted GATC overhangs were generated by annealing the modified strand to complementary strands that generate caps for substrate head and tail ends. Head and tail caps have a 5′-phosphotyrosine-GATC overhang terminus on one end; the 5′-phosphorylated, non-adducted overhangs on the other end are made complementary to the head and tail ends of a 270 bp double stranded core fragment generated by polymerase chain reaction. Ligation of an excess of these caps to the 270 bp fragment generates a 300 bp substrate with 5′-phosphotyrosine end structures as described in Figure 7. Unligated caps are removed using a Qiaquick PCR cleanup kit.

In vitro NHEJ reactions

Purified NHEJ proteins (Ku, XRCC4-ligase IV, XLF) were prepared as previously described (27). End joining reactions were performed using 5 nM DNA substrate, 25 nM Ku, 25 nM XRCC4/LigaseIV complex, 50 nM XLF and hTdp2^{FL} proteins as indicated. Reactions contained 25 mM Tris-HCl pH 7.5, 0.1 mM ethylenediaminetetraacetic acid (EDTA), 2 mM dithiothreitol (DTT), 125 mM KCl, 5 mM $MgCl_2$, 100 μM ATP, 8% (w/v) polyethyleneglycol, 0.05% (w/v) Triton X-100, 50 μg ml^{-1} bovine serum albumin (BSA) and 50 ng supercoiled plasmid DNA. Reactions were carried out in a final volume of 10 μl and incubated at 37°C for 5 min. Reactions were stopped by the addition of 0.1% (w/v) SDS and 5 mM EDTA and analyzed by 5% native PAGE.

Cellular NHEJ assays

Mouse embryo fibroblast (MEF) cells from matched Tdp2$^{+/+}$ and *Tdp2*$^{-/-}$ mice (19) were a gift from F. Cortes-Ledesma, and were immortalized by transformation with a construct that expresses SV40 T-antigen (Addgene #1779). HCT-116 cells and a ligase IV deficient variant were the gift of E. A. Hendrickson (28). The cDNAs with wild-type human Tdp2 and polymorphic variants generated by mutagenesis were introduced into pLX302 (29) (Addgene#25896) to prepare lentivirus. Tdp2$^{-/-}$ cells were infected with lentivirus and bulk cell cultures expressing lentiviral delivered construct purified by treatment with puromycin. Expression of human Tdp2 (hTdp2^{FL}) was validated by Western analysis (12203-1-AP; Proteintech). Fifty nanograms of the 300 bp substrates used in *in vitro* experiments and 2 μg of carrier supercoiled plasmid DNA were introduced into 2 × 10^5 MEF or HCT 116 cells by electroporation (Neon, Invitrogen) using a 10 μl chamber and a single 1350 V, 30 ms pulse. Cells were recovered 1 h later, washed with phosphate buffered saline and DNA purified using a Qiamp DNA mini kit on a Qiacube. NHEJ products were quantified by qPCR and characterized by amplicon sequencing as previously described (27).

Etoposide Clonogenic survival assays

Clonogenic survival assays were carried out by treating log phase cells with Etoposide as described in the legend to Figure 7 before seeding treated and mock treated cells in 10 cm dishes. Colonies formed after 10 days post-treatment were strained using a crystal violet (0.5% w/v) solution. Plates containing a minimum of 50 colonies were counted by hand, and at least three plates were counted for each dose.

QM/MM

In the QM/MM calculation, in addition to the water nucleophile and the putative catalytic Lewis base (Asp272), the side chains of proximal residues (Asn130, Asn274, His236, His326, His359, Ser239 and Glu162), the bound phosphate moiety, the Mg^{2+} and three waters in its coordinate shell are all included in the QM sub-system. In addition, we modeled the position of the Top2 peptide tyrosine based on conformations of the substrate analog.

The QM sub-system of this study consisted of 110 atoms with a zero net charge on the sub-system. QM/MM calculations are performed using Gaussian09.D01 (30). Since the QM sub-system contains a large number of buried atoms and commonly used electrostatic potential fitting schemes to obtain the charge distribution at atomic positions become unreliable for such systems with buried atoms, we have selected the CM5 charge model in the current study to calculate the charges on atomic positions at each step of the QM/MM calculation. This CM5 scheme is an extension to the Hirshfeld population analysis and is adapted to handle buried charges properly. This charge distribution of the QM sub-system was used to evaluate contributions of residues in the MM region to the net stability of the transition and product states as compared to that of the initial reactive state. As reported previously (31), this residue analysis is solely based on the electrostatic energy contributions to the initial, transition and product states. According to this estimation, the residues Arg142, Lys213, Ser235, Asp277, Glu279, Asp292, Glu295, Asp308, Asp343, Arg354 and Trp360 contribute toward the stability of both the transition and product states as compared with the reactant. However, the electrostatic contributions from residues Asp132, Asp135, Glu186, Glu242, Arg247, Thr273, Arg276, Lys299, Lys322, Arg324, Arg327 and Asp358 have the opposite effect toward the stabilities of the transition and product states.

RESULTS

Tdp2 processing of compound DNA damage

Two potent Top2 poisons include bulky alkylated DNA helix-distorting DNA base adducts (e.g. 1-N^6-ethenoadenine, ϵA) (16) and abundant abasic sites (13) (Figure 1A). Whether Tdp2 processes phosphotyrosyl linkages within these diverse structural contexts is not known. To test this, we adapted an EDC coupling method to generate 5′-terminal *p*-nitrophenol (PNP) modified oligonucleotides (32,33) that also harbored DNA damage at the 5′-nucleotide position (see Materials and Methods). We then evaluated the ability of a recombinant purified mouse Tdp2 catalytic domain (mTdp2^{cat}) to release PNP (a structural mimic of a topoisomerase tyrosine) from the 5′-terminus of compound damaged DNA substrates using a colorimetric assay (Figure 1B). We observe robust Tdp2-dependent release of PNP from 5′-modified oligonucleotides in the context of dA-PNP, ϵA-PNP or the abasic-site analog tetrahydrofuran spacer (THF) (Figure 1C). Thus, Tdp2 efficiently cleaves phosphotyrosyl linkages in the context of a compound 5′ lesions composed of abasic or bulky DNA base adduct DNA damage.

To understand the molecular basis for Tdp2 processing of Top2cc in the context of DNA damage, we crystallized and determined X-ray crystal structures of mTdp2^{cat} bound to 5′-phosphate DNA (product complex) with a 5′-ϵA at 1.43 Å resolution (PDB entry 5HT2) and the abasic DNA damage mimic 5′-THF at 2.15 Å resolution (PDB entry 5INK; Figure 1D and E, Table 1). In these Tdp2-DNA complex structures, mTdp2^{cat} adopts a mixed α-β fold typified by a central 12-stranded anti-parallel β-sandwich enveloped by several helical elements that mold the Tdp2 active site. One half of the molecule contributes to formation of the walls of the DNA-binding cleft that embraces the terminal position of the damaged DNA substrate. In the DNA lesion-bound state, two key DNA binding elements, the β-2-helix-β (β2Hβ) ‘grasp’, and ‘helical cap’ mold the substrate binding trench and direct the ssDNA of a 5′-overhang substrate into the active site. A comparison to an additional new structure of DNA-free Tdp2 (apo state, Figure 1F) shows that this loop is conformationally mobile and important for engaging DNA substrates.

The mode of engagement of the 5′-nucleobase of the bulky ϵA adduct describes a mechanism for Tdp2 to bind 5′-tyrosylated substrates that contain diverse forms of DNA damage. The 5′-ϵA nucleobase is recognized by an extended Tdp2 van Der Waals interaction surface, referred to here as the 'hydrophobic wall' that is assembled with the sidechains of residues Leu315 and Ile317 (Figure 2A and B).

For comparison, we also determined a structure of an undamaged 5′-adenine (5′-dA) bound to Tdp2 at 1.55 Å (PDB entry 5INL). A structural overlay of damaged and undamaged nucleotides shows no major distortions to nucleotide planarity between different bound sequences and DNA damage (compare ϵA, dA and dC, Supplementary Figure S1A–D). Therefore, structurally diverse undamaged or alkylated bases (e.g. ϵG, ϵT) (34,35) could likely be accommodated in the Tdp2 active site via planar base stacking with the active site facing hydrophobic wall of the β2Hβ motif. Likewise, the abasic deoxyribose analog THF substrate binds similar to the alkylated and non-alkylated substrates, but with a slight alteration in the approach of the 5′-terminus (Figure 2C). Interestingly, in the absence of a nucleobase, O4′ of the THF ring adopts a close approach (2.8 Å) to a water molecule that directly participates in the outer sphere single Mg^{2+} ion coordination shell (Figure 2D). This shift is coincident with a small adjustment in the position of the +2 and +3 nucleotides (Supplementary Figure S1E). These collective differences may explain the slight, but statistically significant elevated activity on the THF substrate (Figure 1C).

Structural plasticity in the Tdp2 DNA binding trench

An intriguing feature of the DNA-damage bound conformation of the Tdp2 active site is an underlying network of protein–water–protein contacts that span a gap between the catalytic core and the DNA binding β2Hβ-grasp (Supplementary Figure S2). In this arrangement, six solvent molecules form a channel under the β2Hβ-grasp, ending with hydrogen bonds to the peptide backbone of the Mg^{2+} ligand Asp358. The paucity of hydrophobic interactions stabilizing the β2Hβ DNA-bound conformation suggests that conformational plasticity in the β2Hβ might be a feature of DNA damage and metal cofactor engagement. To test this hypothesis, we crystallized Tdp2 in the absence of DNA and determined a DNA free Tdp2 structure to 2.4 Å resolution (PDB entry 5INM; Figures 1F and 3A).

This crystal form contains 5 Tdp2 protein molecules in the asymmetric unit, with variations in active site Mg^{2+} occupancy and substrate binding loops observed for the individual protomers. The most striking feature of the DNA ligand-free state is that the active site β2Hβ-grasp can adopt alternative structures that are distinct from the DNA-bound, closed β2Hβ DNA binding grasp (Figure 3A and B). In one monomer (chain 'E'), the grasp adopts an 'open' 3-helix loop conformation that projects away from the EEP catalytic core. Two monomers have variable disordered states for which much of the DNA binding loop is not visible in the electron density. The remaining two molecules in the DNA-free crystal form are closed β2Hβ conformers similar to the DNA bound structures (Figure 3C). Thus, we posit that Tdp2 DNA binding conformationally selects the closed form of the β2Hβ grasp, rather than inducing closure upon binding.

A detailed analysis of the extended 3-helix conformation shows that the substrate-binding loop is able to undergo metamorphic structural changes. In this open form, residues Asn312-Leu315 are distal from the active site and solvent-exposed (orange sticks, Figure 3A), while Thr309 (green surface, Figure 3A) packs into a shallow pocket of the EEP core to anchor the loop. Burial of Thr309 is enabled by an unusual main chain *cis*–peptide bond between Asp308-Thr309 and disassembly of the short antiparallel beta-strand of the β2Hβ fold. By comparison, the closed β2Hβ grasp conformer is stabilized by Asn312 and Asn314 binding into two β2Hβ docking pockets, and Leu315 engagement of the 5′-terminal nucleobase (Figure 3B). To transition into the closed β2Hβ conformation, Thr309 disengages from the EEP domain pocket, flips peptide backbone conformation *cis* to *trans*, and is integral to the β2Hβ antiparallel β-sheet. Stabilization of the closed β2Hβ-grasp conformation is linked to the active site through a hydrogen bond between Trp307 and the Mg^{2+} coordinating residue Asp358. Accordingly, in the DNA free structure, we observe a trend where the 2 closed monomers have an ordered Mg^{2+} ion in their active sites, while the monomers with open conformations have a poorly ordered or vacant metal binding site. Overall, these observations suggest that engagement of diverse damaged DNA ends is enabled by an elaborate substrate selected stabilization of the β2Hβ DNA binding grasp, and these rearrangements are coordinated with Mg^{2+} binding in the Tdp2 active site.

To evaluate Mg^{2+} and DNA-dependent Tdp2 structural states in solution, we probed $mTdp2^{cat}$ conformations using limited trypsin and chymotrypsin proteolysis (Figure 3C–E). In the absence of DNA or Mg^{2+}, $mTdp2^{cat}$ is efficiently cleaved in the metamorphic DNA binding grasp at one site by trypsin (Arg316), or at two positions by chymotrypsin (Trp307 and Leu315). By comparison, Mg^{2+}, and to a greater extent Mg^{2+}/DNA mixtures (compare Figure 3, lanes 4, 7 and 13) protect $mTdp2^{cat}$ from proteolytic cleavage. Interestingly, addition of Mg^{2+} alone protects against proteolysis as well. This is consistent with Mg^{2+} stabilizing the closed conformation of the β2Hβ-grasp through an extended hydrogen-bonding network with Asp358 and the indole ring of the β2Hβ-grasp residue Trp307 (also discussion below on Tdp2 active site SNPs).

To assess structural conservation of Tdp2 conformational changes between human and mouse Tdp2, we also determined a 3.2 Å resolution structure of the human $Tdp2^{cat}$ domain bound to a DNA 5′-PO_4 terminus product complex (PDB entry 5INO). Comparisons of the human $hTdp2^{cat}$-DNA complex structure to the $mTdp2^{cat}$ DNA bound state show a high level of conservation of the DNA-bound conformations (Supplementary Figure S3A). Moreover, similar to $mTdp2^{cat}$, proteolytic protection of the $hTdp2^{cat}$ substrate binding loop occurs with addition of Mg^{2+} and DNA (Supplementary Figure S3B). Thus, X-ray structures and limited proteolysis analysis indicate that DNA- and metal-induced conformational changes are a conserved feature of the vertebrate Tdp2-substrate interaction.

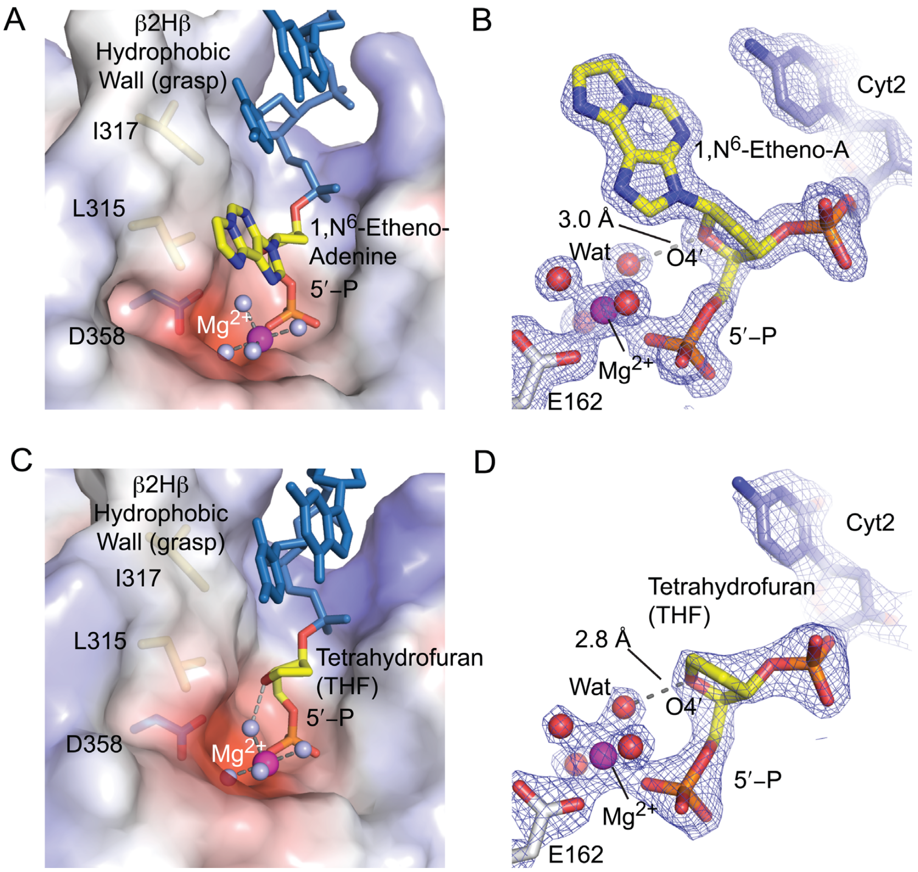

Figure 2. Structures of mTdp2^{cat} bound to DNA damage that triggers Top2 poisoning. (**A**) Structure of mTdp2^{cat} bound to 5′-phosphate DNA (product complex) containing ϵA (yellow), Mg^{2+} (magenta) and its inner-sphere waters (gray). mTdp2^{cat} is colored by electrostatic surface potential (red = negative, blue = positive, gray = neutral/hydrophobic). PDB entry 5HT2. (**B**) σ-A weighted 2Fo-Fc electron density map (at 1.43 Å resolution, contoured at 2.0 σ) for the ϵA DNA complex. The ϵA nucleotide is shown in yellow and a hydrogen bond from the ϵA O4′ to inner-sphere water is shown as gray dashes. (**C**) Structure of mTdp2^{cat} bound to 5′-phosphate DNA (product complex) containing THF (yellow), Mg^{2+} (magenta) and its inner-sphere waters (gray). mTdp2^{cat} is colored with red (electronegative), blue (electropositive) and gray (hydrophobic) electrostatic surface potential displayed. PDB entry 5INK is displayed. (**D**) σ-A weighted 2Fo-Fc electron density map (at 2.15 Å resolution, contoured at 2.0 σ) for THF-DNA complex. The THF is shown in yellow and a hydrogen bond from the THF O4′ to inner-sphere water is shown as gray dashes.

Tdp2 metal ion dependence

Consistently in high-resolution X-ray structural analyses we, (8,20) and others (36) observe a single Mg^{2+} metal bound in the Tdp2 active site. This includes the DNA-free (Figure 3A), DNA damage bound (Figure 3B) and reaction product-bound crystal forms of mouse, (PDB entry 4GZ1), *D. rerio* (PDB entry 4FPV) and *C. elegans* Tdp2 (PDB entry 4FVA). However, previous biochemical analysis has suggested an alternative two-metal ion mechanism for the Tdp2-phosphotyrosyl phosphodiesterase reaction (37). In these experiments, at limiting Mg^{2+} concentrations, Ca^{2+} addition to Tdp2 reactions stimulated activity. While this work was suggestive of a two metal ion mechanism for phosphotyrosyl bond cleavage by Tdp2, we note that second metal ion titrations can be influenced by metal ion binding sites outside of the active site (38). In fact, divalent metals have been observed in the Tdp2 protein–DNA complexes (PDB entry 4GZ2) distal to the active center (20), and we propose this might account for varied results in different studies. To further probe the metal ion dependence of the Tdp2 phosphodiesterase reaction, we performed metal ion binding assays, determined crystal structures in the presence of varied divalent metals (Mn^{2+} and Ca^{2+}), and analyzed metal ion dependence of the Tdp2 phosphotyrosyl phosphodiesterase reaction (Figure 4).

Our proteolysis results indicate a Mg^{2+}-dependent Tdp2 conformational response to metal binding. The Tdp2 active site has three tryptophan residues within 10 Å of the metal binding center, so we assayed intrinsic tryptophan fluorescence to detect metal-induced conformational changes in mTdp2^{cat}. These data were an excellent fit to a single-site binding model both in the presence and absence of DNA (Figure 4A). This analysis revealed Mg^{2+} K_d values in the sub-millimolar range and Hill coefficients which were consistent with a single metal binding site both in the presence and absence of DNA (Supplementary Table S2). We then measured effects of metal ion concentrations on Tdp2 cleavage of *p*-nitrophenyl-thymidine-5′-phosphate by mTdp2^{cat} (20,39). This small molecule substrate is not expected to be influenced by metal–DNA coordination outside of the active site. Inclusion of ultrapure Ca^{2+} (1 mM or 10 mM) results in a dose-dependent inhibition but not stimulation Tdp2 activity, even in conditions of limiting

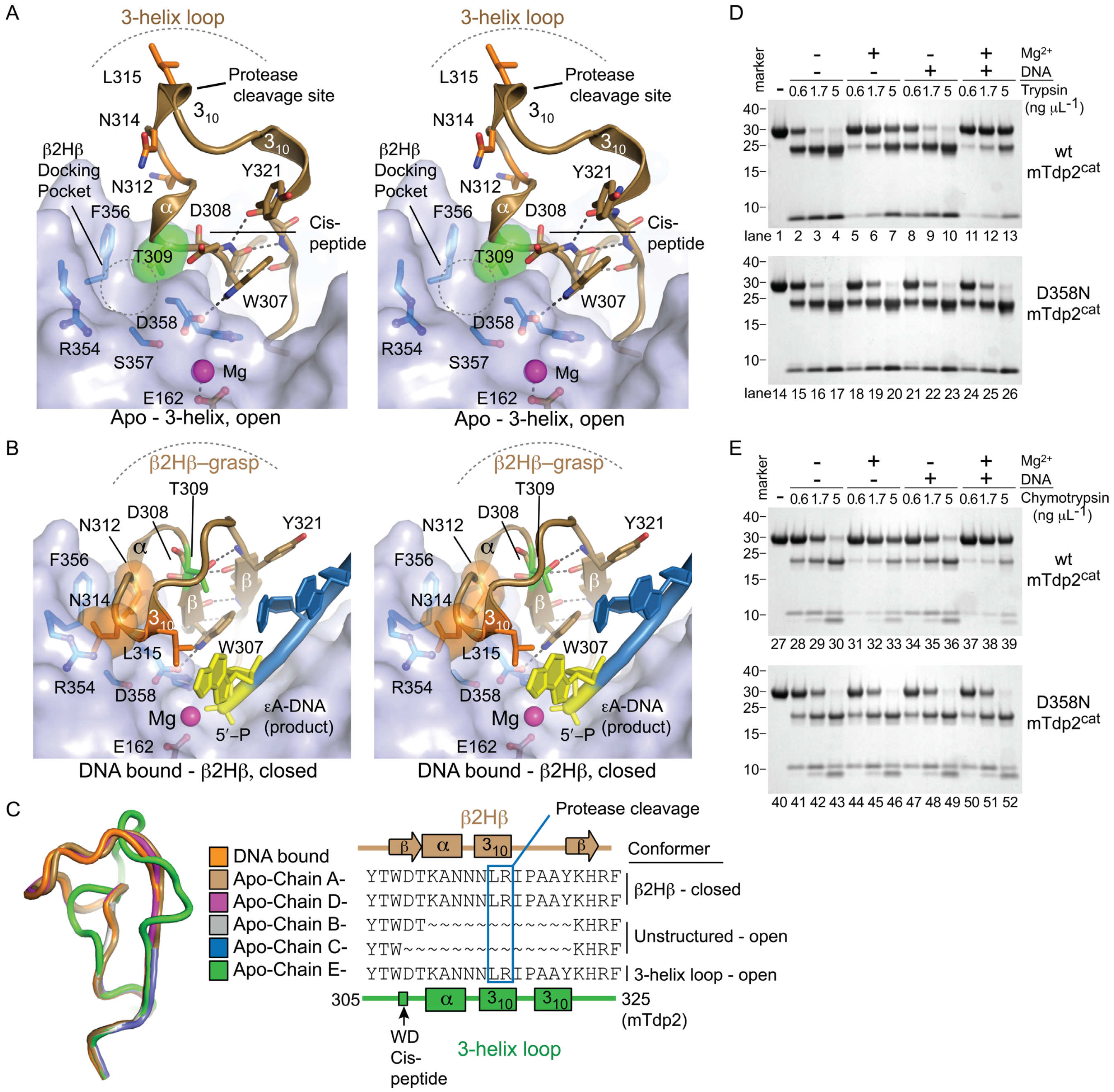

Figure 3. Conformational plasticity in the Tdp2 active site. (**A**) The open, 3-helix conformation (tan) of flexible active-site loop observed in monomer E of the DNA-free mTdp2^{cat} structure (PDB entry 5INM) is supported by T309 (green), which packs against the EEP core. The β2Hβ docking pocket (circled) is unoccupied and residues N312, N314 and L315 (orange) are solvent-exposed. Wall-eyed stereo view is displayed. (**B**) The closed β2Hβ conformation in the mTdp2^{cat}–DNA product structure containing 5′-ϵA (yellow, PDB entry 5HT2). T309 (green) is an integral part of the β2Hβ DNA-binding grasp (tan) and hydrogen bonds to the backbone of Y321, while N314 (orange) occupies the β2Hβ docking pocket. Wall-eyed stereo view is displayed. (**C**) Alignment of active site loop conformers observed in the 5 promoters of the DNA-free mTdp2^{cat} (PDB entry 5INM, see Table 1) crystallographic asymmetric unit (left) and sequence alignment showing residues not observed in the electron density as '∼' (right). (**D**) Limited trypsin proteolysis probes the solvent accessibility of the flexible active-site loop. mTdp2^{cat} WT (lanes 1–13) or mTdp2^{cat} D358N (lanes 14–26) were incubated in the presence or absence of Mg^{2+} and/or a 12 nt self annealing, 5′-phosphorylated DNA (substrate '12 nt' in Supplementary Table S1), then reacted with 0.6, 1.7 or 5 ng μl^{-1} of trypsin. Reactions were separated by SDS-PAGE and proteins visualized by staining with coomassie blue. (**E**) Limited chymotrypsin proteolysis probes the solvent accessibility of the flexible active-site loop. Experiments performed as in panel D for mTdp2^{cat} WT (lanes 27–39) or mTdp2^{cat} D358N (lanes 40–52), but with chymotrypsin instead of trypsin.

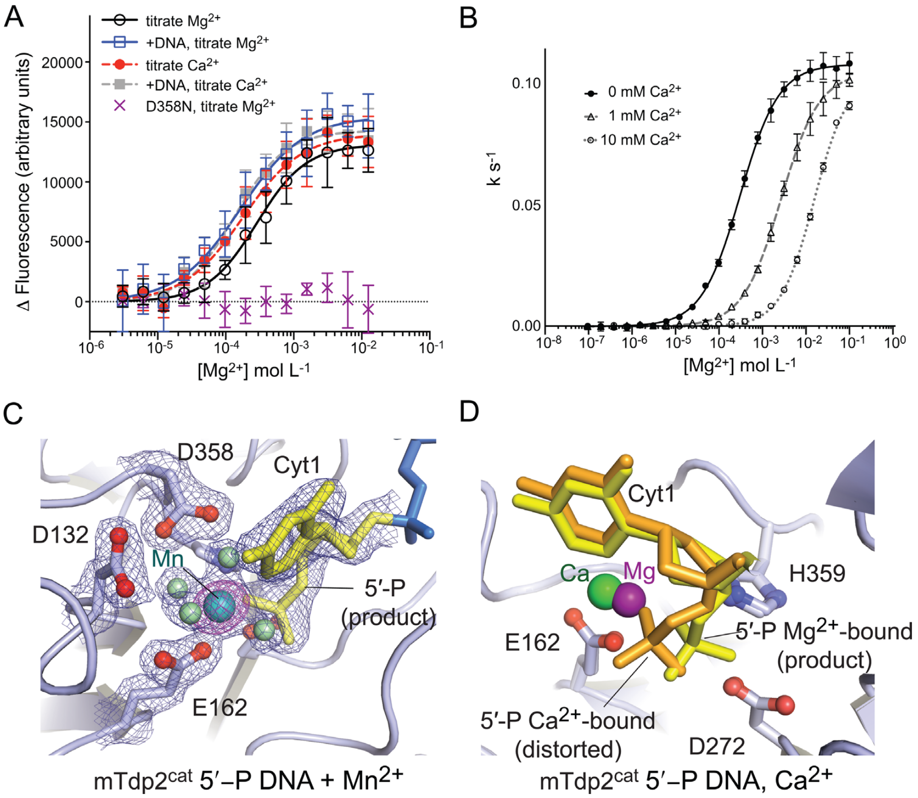

mTdp2^{cat} 5′–P DNA + Mn^{2+}

mTdp2^{cat} 5′–P DNA, Ca^{2+}

Figure 4. Metal cofactor interactions with Tdp2. (**A**) Intrinsic tryptophan fluorescence of mTdp2^{cat} was used to monitor a conformational response to divalent metal ion binding. Either Mg^{2+} or Ca^{2+} were titrated in the presence or absence of 5′-P DNA, and the tryptophan fluorescence was monitored with an excitation wavelength of 280 nm and emission wavelength of 350 nm using 10 nm band pass filters. Both Mg^{2+} and Ca^{2+} induce a conformational change which elicits an increase in tryptophan fluorescence of mTdp2^{cat} in the presence and absence of DNA, while D358N active site mutant of mTdp2^{cat} is unresponsive to Mg^{2+}. (**B**) mTdp2^{cat} activity assayed on a T5PNP substrate as a function of Mg^{2+} and Ca^{2+} concentration. PNP release (monitored by absorbance at 415 nm) as a function of Mg^{2+} concentration and in the absence or presence of 1 or 10 mM Ca^{2+} is shown; error bars, s.d. n = 4. (**C**) σ-A weighted 2Fo-Fc electron density map (blue) and model-phased anomalous difference Fourier (magenta) maps for the mTdp2^{cat}–DNA–Mn^{2+} complex (PDB entry 5INP) show a single Mn^{2+} (cyan) is bound with expected octahedral coordination geometry. A 53σ peak in the anomalous difference Fourier map (data collected at $\lambda = 1.5418$ Å) supports Mn^{2+} as the identity of this atom. (**D**) Comparison of Ca^{2+} (green Ca^{2+} ion, orange DNA) (PDB entry 5INQ), and Mg^{2+} (magenta Mg^{2+} ion, yellow DNA) (PDB entry 4GZ1) mTdp2^{cat}–DNA structures shows that Ca^{2+} distorts the 5′-phosphate binding mode.

Mg^{2+} (Figure 4B). We performed the same titrations with human hTdp2^{FL} and hTdp2^{cat} (Supplementary Figure S4), and find similar stimulation of activity by Mg^{2+} and inhibition by Ca^{2+}. Overall, these metal binding analyses are consistent with a single metal ion mediated reaction.

To further evaluate the structural influence of divalent cations on the Tdp2 active site, we determined crystal structures by soaking crystals with metal cofactors that either support (Mn^{2+}) (20) or inhibit (Ca^{2+}, Figure 4B) the Tdp2 reaction (PDB entries 5INP and 5INQ). Anomalous difference Fourier maps of the Tdp2–DNA–Mn^{2+} complex show a single binding site for Mn^{2+} in each Tdp2 active site (Figure 4C), with octahedral coordination and bond lengths typical for Mn^{2+} ligands (Supplementary Table S3). The Mn^{2+} ion is positioned in the Tdp2 active site similar to the Mg^{2+}-bound complex (Figure 2C), which is consistent with the ability of Mn^{2+} to support robust Tdp2 catalytic activity (20). In contrast, while co-complex structures with Ca^{2+} also show a single metal ion, Ca^{2+} binds in a slightly different position, shifted ~1 Å from the Mg^{2+} site. Although Ca^{2+} is also octahedrally coordinated, longer bond lengths for the Ca^{2+} ligands (Supplementary Table S3) shift the Ca^{2+} ion relative to the Mg^{2+} ion site. Interestingly, bidentate inner sphere metal contacts from the Ca^{2+} ion to Glu162 distort the active site phosphate-binding mode, and dislodge the 5′-PO$_4$ out of the Tdp2 active site (Figure 4D). Together with results showing that under the conditions examined here, Ca^{2+} inhibits rather than stimulates the Tdp2 reaction, the divalent metal bound Tdp2 structures provide a mechanism for Ca^{2+}-mediated inhibition of the Tdp2 reaction.

Modeling the Tdp2 reaction coordinate

Next, to examine the feasibility of our proposed single Mg^{2+} mechanism, we simulated the Tdp2 reaction coordinate with hybrid QM/MM modeling using Tdp2 substrate analog- and product-bound structures as guides. Previous structural analyses showed that the superposition of a DNA substrate mimic (5′-aminohexanol) and product (5′-PO$_4$) complexes delineates a probable Tdp2 reaction trajectory characterized by inversion of stereochemistry about the adducted 5′-phosphorus (20). In this scheme (Figure 5A), a candidate nucleophilic water that is strongly hydro-

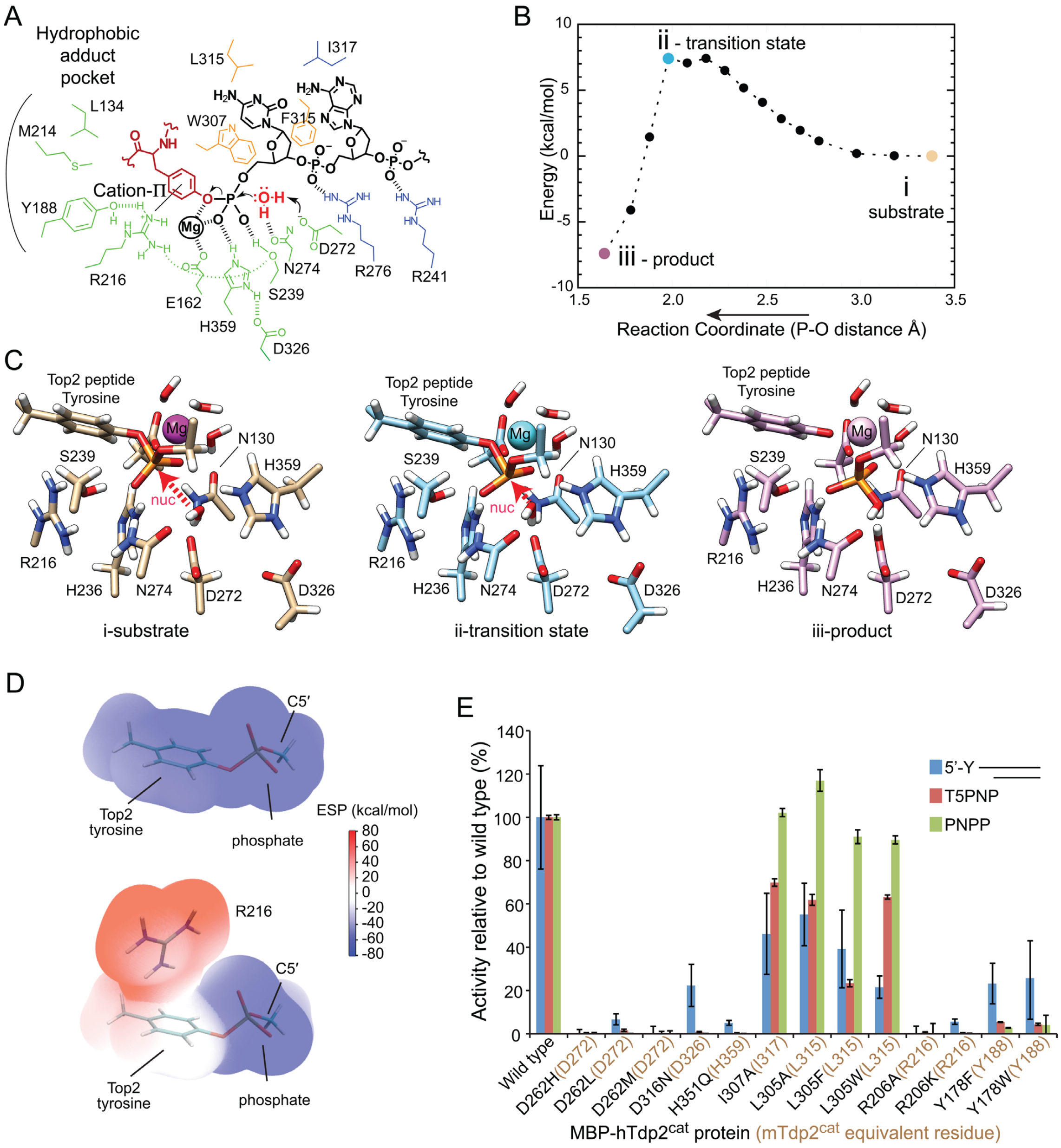

Figure 5. Structure-function analysis of the Tdp2 reaction mechanism. (**A**) Proposed mechanism for hydrolysis of phosphotyrosine bond by Tdp2. Residues in green form the binding-site for the 5′-tyrosine (red) and phosphate, yellow bind the 5′ nucleotide and blue bind nucleotides 2–3. Residue numbers shown are for the mTdp2 homolog. (**B**) Free energy during the QM/MM simulation as a function of distance between the nucleophilic water and 5′-phosphorus atom. Reaction proceeds from right to left. (**C**) Models for the mTdp2^{cat}-DNA complex during the QM/MM reaction path simulation showing the substrate (left, tan), transition state intermediate (center, cyan) and product (right, pink) states. Residue numbers shown are for the mTdp2 homolog. (**D**) Electrostatic surface potential calculated for 5′-phosphotyrosine in isolation (upper panel) and in the presence of a cation–π interaction with the guanidinium group of Arg216 (lower panel) shows electron-withdrawing effect of this interaction. Electrostatic potential color gradient extends from positive (red) through neutral (gray), to negative (blue). (**E**) Bar graph displaying the relative activity of wild-type and mutant human MBP-hTdp2^{cat} fusion proteins on the three substrates. Release of PNP from PNP phosphate and T5PNP was detected as an increase in absorbance at 415 nm. Reaction rates are expressed as the percent of activity relative to wildtype MBP-hTdp2^{cat}; error bars, s.d. n = 3. Mutants of hTdp2 (black) and the equivalent residue in mTdp2 (tan) are indicated.

gen bonded to Asp272 and Asn274, is well positioned for the in-line nucleophilic attack ~180° opposite of the P–O bond of the 5′-Tyr adduct.

We examined the energy profile of the nucleophilic attack of the water molecule by using the distance between the water oxygen and the P atom on the phosphate moiety as the sole reaction coordinate in the present calculation (Figure 5B and C). A starting model was generated from atomic coordinates of the mTdp2^{cat} 5′–aminohexanol substrate analog structure (PDB 4GZ0) with a tyrosine replacing the 5′-aminohexanol then adding the Mg^{2+} and inner-sphere waters from the mTdp2-DNA product structure (PDB, 4GZ1), and running an initial round of molecular dynamics simulation (10 ns) to allow the system to reach an equilibrium.

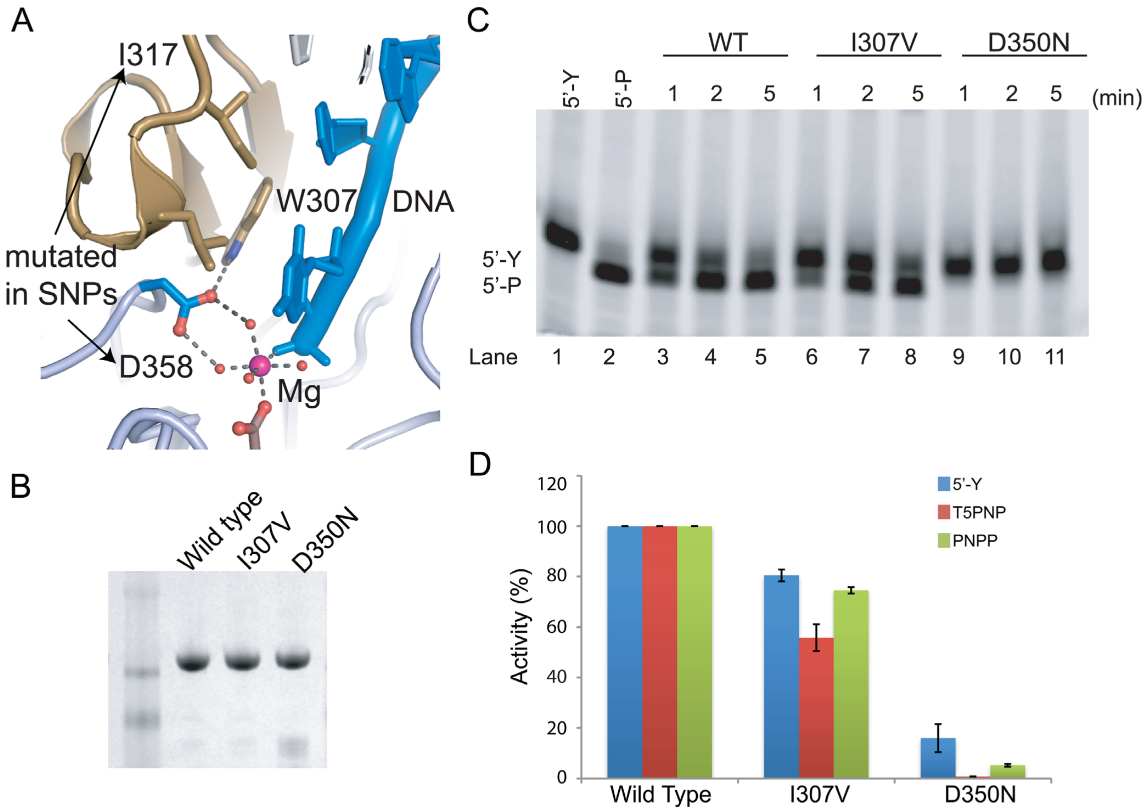

Figure 6. Tdp2 SNPs impair function. (**A**) Active site residues mutated by *TDP2* SNPs. D350N (mTdp2 D358N) and I307V (mTdp2 I317V) substitutions are mapped onto the Tdp2 active site of the high-resolution mTdp2^{cat} structure (4GZ1). (**B**) Coomassie blue stained SDS-PAGE gel of purified WT and mutant MBP-hTdp2^{cat} proteins used for assays in panels C and D. (**C**) Activity of WT and mutant MBP-hTdp2^{cat} proteins on a 5′–phosphotyrosyl–DNA oligonucleotides with 3′-fluorescein label. Samples were withdrawn from reactions, neutralized with TBE-urea loading dye at the indicated timepoints, and electrophoresed on a 20% TBE-urea PAGE. (**D**) Relative activity of WT and indicated mutant human MBP-hTdp2^{cat} fusion proteins on three model Tdp2 substrates. Quantification of percent MBP-hTdp2^{cat} activity relative to WT protein for the 5′-Y DNA oligonucleotide substrate (blue bars), T5PNP (red bars) and PNPP (green bars) is displayed. Release of PNP from PNP phosphate (PNPP) and was detected as an increase in absorbance at 415 nm, whereas the 5′-Y substrate is quantification of activity in a gel based assay shown in Figure 6C. Error bars, s.d. n = 3.

After QM/MM optimization of this model (Figure 5C, 'i-substrate'), the O–P distance is 3.4 Å, which is in agreement with the range of distances observed in the mTdp2^{cat} 5′-aminohexanol substrate analog structure (3.2–3.4 Å). No appreciable energy penalty is observed during the first 0.5 Å of the reaction coordinate. When the reaction reaches an O–P distance of 2.18 Å, formation of a transition state with an energy maximum of +7.4 kcal mol^{-1} is observed. Here, the water proton and the neighboring O of Asp272 participates in a strong hydrogen bond (distance of 1.58 Å) and the phosphotyrosyl O–P distance is stretched to 1.77 Å, which is 0.1 Å beyond an equilibrium bond length. In the subsequent two steps of the simulation, as the water-phosphate O–P distance reduces to 1.98 Å, a key hydrogen bond between the nucleophilic water and Asp272 shortens to 1.38 Å as the water H–O bond approaches the point of dissociation. The second proton on the water nucleophile maintains a strong hydrogen bond with Asn274 throughout the reaction, implicating this residue in orienting the water nucleophile during the reaction. Concomitant with this, the phosphotyrosyl O–P bond weakens (d = 1.89 Å), and the formation of the penta-covalent transition state (Figure 5C 'ii-transition state') is observed. The final steps show inversion of stereochemistry at the phosphate, along with lengthening and breaking of the phosphotyrosyl O–P bond. Product formation is coupled to a transfer of a proton from the nucleophillic water to Asp272, consistent with the proposed function for this residue as the catalytic base.

Of note, both nitrogens of the imidazole side chain of His 359 require protonation for stability of the simulation. Asp 326 makes a hydrogen bond to N∂1 of His359, suggesting that this salt bridge could stabilize the protonated form of His359 as has been demonstrated for the analogous Asp-His pair in the EEP domain of APE1, which elevates the pK$_a$ of this His above 8.0 (40). In our model, the transition state contains a hydrogen bond between the doubly protonated His359 and the phosphate oxygen that also coordinates with the single catalytic Mg^{2+}, while the second His359 imidazole proton maintains a H-bond with the Asp326 residue throughout the reaction. In the final optimized structure, the observed product state (Figure 5C, 'iii-product') is found in a conformation that is 7.4 kcal mol^{-1} more stable than the initial reactive state (Figure 5B).

The tyrosine oxy-anion product is coordinated to the Mg^{2+} ion with a 2.0 Å distance, which is the shortest of the six Mg^{2+} ligands (including three water molecules, one of the free oxygens on the phosphate group and the Glu162 residue), indicating the single Mg^{2+} greatly stabilizes the

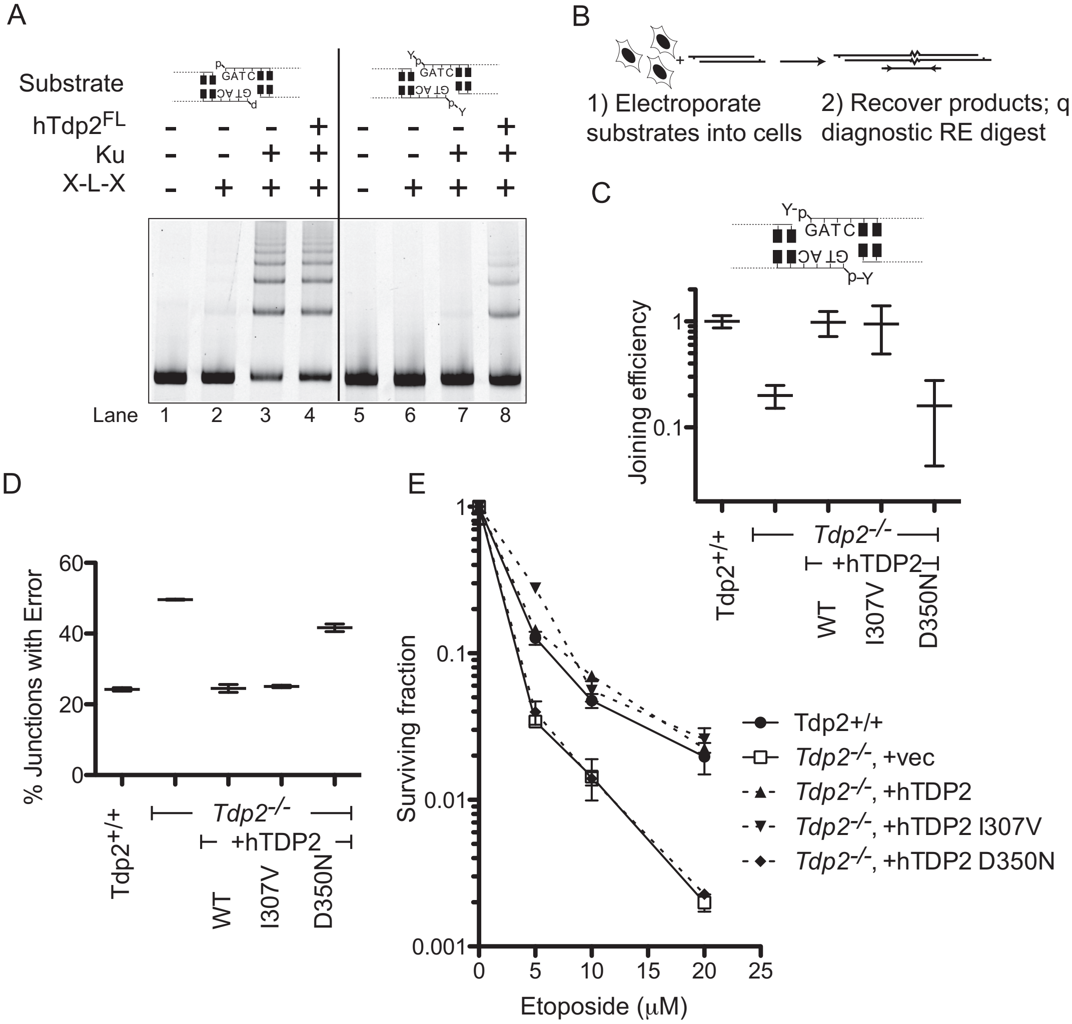

Figure 7. Effects of Tdp2 active site SNP-encoded mutants on cellular Tdp2 functions. (**A**) Cy5 labeled substrates with 5′-phosphate termini (*Lanes 1–4)* or 5′-tyrosylated termini (*Lanes 5–9)* were incubated with Ku, the NHEJ ligase (XRCC4, ligase IV and XLF; X-L-X) and 1 nM hTdp2^{FL} as indicated (+) for 5 min at 37°C. Concatemer ligation products were detected by 5% native PAGE. (**B**) Workflow diagram of cellular end joining assays. DNA substrates with 5′-phosphotyrosine adducts and 4 nucleotide 5′ overhangs were electroporated into cultured mammalian cells. After 1 h, DNA was recovered from cells and repair efficiency by qPCR or sequencing as indicated. (**C**) qPCR assessment of cellular end joining efficiency of the tyrosylated substrate comparing results from wildtype MEF cells to *Tdp2*$^{-/-}$ cells and *Tdp2*$^{-/-}$ cells complemented with wildtype or the noted hTDP2^{FL} variants; Joining efficiency shown is the ratio of junctions recovered relative to WT cells. Error bars, s.d, n = 3. (**D**) Junctions recovered from cellular end-joining assays in the noted cell types were characterized by sequencing to assess the end-joining error rate. Error bars, s.d, n = 3. (**E**) Clonogenic survival assay of WT, Tdp2 knockout and complemented MEF cells after treatment with indicated concentrations of etoposide for 3 h; error bars, s.d, n = 3.

product oxy-anion. An additional striking feature gleaned from the QM/MM modeling is the putative binding mode of the Top2 tyrosine-leaving group. A trio of conserved residues (Tyr 188, Arg 216 and Ser 239) forms the walls of a conserved Top2 tyrosine binding pocket. We propose this cation–π interaction further contributes to tuned stabilization of the negatively charged phenolate reaction product. Consistent with this, analysis of electrostatic potential of the phosphotyrosyl moiety using Gaussian 09.D01 (30) in the presence and absence of the Arg216 guanidinium reveals Arg216 is strongly electron withdrawing (Figure 5D). We further examined the contribution of this cation–π interaction to the reaction chemistry by moving the guanidinium group of Arg216 from the QM system to the MM system as either a +1 or ~0 charge species, and re-computed energy penalties for each step in the reaction coordinate (Supplementary Figure S5A). Removing Arg216 from the quantum subsystem incurs an ~2 kcal mol^{-1} penalty in the transition state and product complex. Removing the +1 charge on the Arg216 has a minimal impact on the transition state, but incurs an additional ~2 kcal mol^{-1} penalty in the product complex. Altogether, QM/MM modeling identifies new determinants of the Tdp2 reaction, and demonstrates our proposed single Mg^{2+} catalyzed reaction model is a viable mechanism for Tdp2-catalyzed 5′-phosphotyrosine bond hydrolysis.

Tdp2 mutational analysis

To test the aspects of the Tdp2 reaction mechanism described here derived from high-resolution mouse Tdp2 crystal structures (denoted with superscript numbering 'm' for numbering of the mouse protein), we engineered and purified thirteen human MBP-hTdp2^{cat} mutant proteins (denoted with superscript numbering and 'h' for the human protein) and assayed the impacts of mutations on Tdp2 catalytic activity using three *in vitro* reporter substrates including a tyrosylated DNA substrate (5′-Y), *p*-nitrophenyl phosphate (PNPP) and thymidine 5′-monophosphate *p*-nitrophenyl ester (T5PNP) (20) (Figure 5E, Supplementary Figures S5B and S5C). By analyzing activities on this nested set of chemically related substrates we aimed to dissect structure-activity relationships of Tdp2 catalysis. For example, mutations impacting Tdp2 active site chemistry and phosphotyrosyl bond cleavage should similarly affect catalysis on all three substrates, but mutants impacting DNA damage binding might only impair catalysis on 5′-Y and T5PNP but not PNPP that lacks a nucleobase.

Structural results and QM/MM modeling indicate ^{m}Asp272 activates a water molecule for in-line nucleophilic attack of the scissile phosphotyrosyl linkage. To test if this proposed Lewis base is critical for reaction chemistry we mutated it to a His, which could alternatively support metal binding, as well as bulky hydrophobic residues (Leu and Met) that we predict would block the water-binding site. Similar to a previously characterized ^{h}D262N mutation (20), all three substitutions ablate activity, supporting essential roles for ^{h}Asp262 (^{m}Asp272) in catalysis. Next, we mutated key elements of the mobile loop (β2Hβ hydrophobic wall, Figure 2A and C). Mutations ^{h}I307A, ^{h}L305A, ^{h}L305F and ^{h}L305W all impaired catalysis on both nucleotide-containing substrates (<50% activity). The ^{h}L305W substitution that we expect to have the most distorting impact on conformation of the β2Hβ hydrophobic wall also has the largest impact on catalysis of the DNA substrate 5′-Y. By comparison, as predicted by our model where β2Hβ dictates key interactions with undamaged and damaged nucleobases, all of these substitutions have little impact on PNPP (>90% activity). Third, we altered properties of the proposed enzyme substrate cation–π interface. No activity was detected for a mutant that removes the positive charge at this position (^{h}R206A). The precise geometry of this pocket is also critical for catalysis as replacement of ^{h}Arg206 (^{m}Arg216) with a lysine also results in a profound decrease in catalysis (<5% activity on 5′-Y, no detectable activity on T5PNP or PNPP). Similarly, mutation of ^{h}Tyr178 that structurally scaffolds the ^{h}Arg206 (^{m}Arg216) guanidinium also significantly impacts activity, with Y178F and Y178W having <25% activity on all substrates. Fourth, we evaluated roles for the ^{h}His351–^{h}Asp316 (^{m}Asp326–^{m}His359) transition state stabilization charge pair. We found that mutations that removed the charge yet retained the ability to hydrogen bond (^{h}H351Q) or should abrogate the elevated pK_a of the Histidine (^{h}D316N) had severe impacts on catalysis. Thus altogether, our mutational data support key roles for the active site Lewis base aspartate, mobile substrate engagement loops, enzyme–substrate cation–π interactions, and active site transition state stabilizing charge interaction in supporting Tdp2 catalysis.

A Tdp2 active site single nucleotide polymorphism impairs Tdp2 function

Recently, it was found that inactivation of *TDP2* by a splice-site mutation is associated with neurological disease and confers hypersensitivity to Top2 poisons (18). We considered whether human SNPs causing missense mutations might also impact Tdp2 DNA–protein crosslink repair functions established here as well as Tdp2-mediated NHEJ of blocked DNA termini. We identified two SNPs in human *TDP*2 curated in the NCBI SNP database (41) that result in missense mutations within the DNA processing active site: rs199602263 (minor allele frequency 0.0002), which substitutes ^{h}Asp350 for Asn, and rs77273535 (minor allele frequency 0.004, which substitutes ^{h}Ile307 for Val) (Figure 6A). We show the ^{h}D350N substitution severely impairs activity on all substrates tested *in vitro*, whereas ^{h}I307V only has a mild impact on catalysis (Figure 6B–D). To better understand the basis for the D350N catalytic defect, we analyzed the structural environment of this substitution based on the high-resolution structures of mTdp2^{cat} (Figure 6A). Interestingly, the Tdp2 single Mg^{2+} ion octahedral coordination shell also involves an extended hydrogen-bonding network mediated by ^{h}Asp350 (^{m}Asp358) that stabilizes the DNA-bound conformation of the β2Hβ substrate-binding loop through hydrogen bonding to ^{m}Trp307. Here, ^{h}Asp350 (^{m}Asp358) serves as a structural nexus linking active site metal binding to substrate binding loop conformations.

To define the molecular basis for the ^{h}D350N (^{m}D358N) defect, we crystallized and determined the structure of the DNA-free form of the ^{m}D358N protein to 2.8Å resolution (PDB entry 5INN). This structure shows the D358N mutation disrupts the hydrogen bond between Asp358 and Trp307, shifts the position of Asn358 and destabilizes Trp307. Consequently, poor electron density is visible for the β2Hβ loop which is mostly disordered (Supplementary Figure S6). Although Mg^{2+} is present at the same concentration as the WT-mTdp^{cat} crystals (10 mM), we find the metal site is unoccupied in the ^{m}D358N crystals. Therefore, metal-regulated opening/closure of the active site may modulate Tdp2 activity, and D350N is sufficient to block both metal binding and conformational change. In support of this, we also find that ^{h}D350N (^{m}D358N) impairs Mg^{2+} binding as measured by intrinsic tryptophan fluorescence (Figure 4A), and abrogates Mg^{2+}-stimulated active site conformational changes detected by trypsin and chymotrypsin sensitivity of the Tdp2 metamorphic loop (Figure 3D).

Tdp2 facilitates NHEJ repair of 5′-phosphotyrosine adducted DSBs

Overall, our Tdp2 structure/activity studies reveal a tuned, 5′-detyrosylation DNA end processing activity and it has been demonstrated that Tdp2 could enable repair of Top2 damage by the non-homologous end-joining (NHEJ) pathway (19). Accordingly, we demonstrate here that 5′-tyrosylated ends are sufficient to severely impair an *in vitro* reconstituted mammalian NHEJ reaction (Figure 7A, lanes 3 and 6), unless supplemented with catalytic quantities of hTdp2^{FL} (Figure 7A, lane 8). Interestingly, hTdp2^{cat} is slightly more effective than hTdp2^{FL} in promoting NHEJ of adducted ends, while a catalytically deficient E152Q mutant was inactive in this assay, supporting the notion that Tdp2 catalytic activity is required to support NHEJ of phosphotyrosyl blocked DSBs (Supplementary Figure S7A). We confirmed that efficient joining of the same tyrosine-adducted substrate in cells (Figure 7B) was dependent on both NHEJ (reduced over 10-fold in ligase IV deficient HCT 116 cells; Supplementary Figure S7B), and Tdp2 (reduced 5-fold in Tdp2 deficient MEFs; Figure 7C). Moreover, products with error (i.e. junctions have missing sequence flanking the adducted terminus) are twice as frequent in cells deficient in Tdp2 (Figure 7D). Therefore, in accord with previous work (19), joining of tyrosine adducted ends after Tdp2-mediated detyrosylation is both more efficient and more accurate than joining after endonucleolytic excision (e.g. mediated by Artemis or the Mre11/Rad50/Nbs1 complex).

We next compared the ability of wild-type and mutant hTdp2^{FL} variants to complement Tdp2 deficient mouse embryonic fibroblasts (Supplementary Figure S7C). Joining of extrachromosomal DNA with phosphotyrosine blocked ends, both in terms of efficiency (Figure 7C) and fidelity (Figure 7D), was indistinguishable comparing MEFs from a wild-type mouse, MEFs from a Tdp2-/- mouse overexpressing wild-type human Tdp2, and Tdp2 -/- MEFs overexpressing the I307V variant human Tdp2. In contrast, joining of 5′ phosphotyrosine-blocked ends was reduced 5-fold in Tdp2-/- MEFs, and an equivalent defect was observed in Tdp2-/- MEFs overexpressing Tdp2 D350N. Moreover, the frequency of inaccurate repair was 2-fold higher in both Tdp2 deficient cells and Tdp2 deficient cells overexpressing D350N, relative to cells expressing wild type Tdp2 or hTdp2 I307V (Figure 7D). Expression of wild type or I307V human Tdp2 in Tdp2-/- MEFs was also sufficient to confer levels of resistance to etoposide comparable to the matched wild-type MEF line, while overexpression of human D350N Tdp2 had no apparent complementation activity (Figure 7E). The rare D350N variant is thus inactive by all metrics analyzed. By comparison the more frequent I307V has only mild effects on *in vitro* activity, and no detectable impact on cellular assays.

DISCUSSION

Top2 chemotherapeutic agents remain frontline treatments, and exposure to the chemical and damaged DNA triggers of Top2-DNA protein crosslink formation are unavoidable (3,5,35). Understanding how cells cope with complex DNA breaks bearing topoisomerase–DNA protein crosslinks is key to deciphering individual responses to chemotherapeutic outcomes and genotoxic agents that poison Top2. Together with mutagenesis and functional assays, our new Tdp2 structures in the absence of ligands and in complex with DNA damage reveal four novel facets of Tdp2 DNA-protein conjugate processing: (i) The Tdp2 active site is well-suited for accommodating a variety of DNA structures including abasic and bulky alkylated DNA lesions that trigger Top2 poisoning, (ii) High-resolution structural analysis coupled with mutational studies and QM/MM molecular modeling of the Tdp2 reaction coordinate support a single metal-ion mechanism for the diverse clade of EEP domain catalyzed phosphoryl hydrolase reactions, (iii) The Tdp2 active site is conformationally plastic, and undergoes intricate rearrangements upon DNA and Mg^{2+} cofactor binding and (iv) Naturally occurring Tdp2 variants undermine Tdp2 active site chemistry, cellular and biochemical activities. This mechanistic dissection of Tdp2 interactions with damaged DNA and metal cofactor provides a detailed molecular understanding of the mechanism of Tdp2 DNA protein crosslink processing.

Tdp2 was originally identified as a protein conferring resistance to both Top1 and Top2 anti-cancer drugs (17), however it is hypothesized that the predominant natural source of substrates for Tdp2 are likely the potent DNA damage triggers of Top2 poisoning and Top2 DNA protein crosslinks encountered during transcription (18). The properties of complex DNA strand breaks bearing Top2-DNA protein crosslinks necessitate that Tdp2 accommodates both damaged nucleic acid as well as the topoisomerase protein in its active site for catalysis. The Tdp2 substrate interaction groove facilitates DNA-protein conjugate recognition in two important ways. First, the nucleic acid binding trench is assembled by a dynamic β2Hβ DNA damage-binding loop that is capable of recognizing and processing diverse phosphotyrosyl linkages even in the context of bulky adducts such as ϵA. This is achieved by binding of nucleic acid 'bases out' by an extended base-stacking hydrophobic wall of the β2Hβ-loop. Secondly, our QM/MM analysis further highlights an enzyme–substrate cation–π interaction as an additional key feature of the Tdp2 protein–DNA crosslink binding and reversal. The strictly conserved active site Arg216 appears optimally positioned to stabilize a delocalized charge on the phenolate product of the phosphotyrosyl cleavage reaction through molecular orbital overlap and polarization of the leaving group. To our knowledge, this is the first proposed example of a substrate cation–π interface exploited to promote a phosphoryl-transfer reaction. This unique feature likely provides an additional level of substrate-specificity for Tdp2 by restricting activity to hydrolysis of aromatic adducts characteristic of Top2cc, picornaviral protein–RNA (42) and Hepatitis B Virus (HBV) protein–DNA processing intermediates (43). By comparison, other EEP nucleases such as Ape1 (44) and Ape2 (45) have evolved robust DNA damage specific endonucleolytic and exonucleolytic activities not shared with Tdp2.

The dynamic nature of the Tdp2 active site presents opportunities for enzyme regulation. However, whether additional protein factors can bind to Tdp2 and modulate assembly/disassembly of the Tdp2 β2Hβ-loop is unknown. We hypothesize that binding of the Top2 protein component of a DNA–protein crosslink and/or other protein-regulated assembly of the Tdp2 active site might also serve to regulate Tdp2 activity to restrict it from misplaced Top2 processing events, such that it cleaves only topologically trapped or poisoned Top2 molecules when needed. Furthermore, high-resolution structures of mouse (20) (Figures 3 and 4) and *C. elegans* (36) Tdp2 show that a single metal ion typifies the Tdp2 active site from worms to man. Herein, we report five additional lines of evidence from metal binding detected by intrinsic tryptophan fluorescence, crystallographic analysis of varied metal cofactor complexes, mutagenesis, Ca^{2+} inhibition studies and QM/MM analysis that all support a feasible single Mg^{2+} mediated Tdp2 catalytic mechanism.

The advent of personalized medical screening opens doors for assessment of individual vulnerabilities to commonly used chemotherapeutic drugs. It would be beneficial to employ this knowledge during the early decision making processes regarding treatment. Etoposide and other Top2 poisons remain front line anti-cancer drugs (4), and Tdp2 frameshift mutations in the human population confer hypersensitivity to Top2 poisons including etoposide and doxyrubicin (18). Given Tdp2 variation in the human population, links to neurological disease (18) and viral pathogenesis (42), our finding that *TDP2* SNPs ablate catalytic activity has probable implications for modulation of cancer chemotherapy, susceptibility to environmentally linked Top2 poisons, and viral infection. Lastly, Tdp2 inhibitors may synergize or potentiate cytotoxic effects of current anticancer treatments that target Tdp2. Thus, we anticipate this atomic-level and mechanistic definition of the molecular determinants of Tdp2 catalysis and conformational changes driven by DNA–protein and protein–protein interactions will foster unique strategies for the development of Tdp2 targeted small molecule interventions.

ACCESSION NUMBERS

Coordinates and structure factors have been deposited in the RCSB Protein Data Bank under accession code 5HT2 (mTdp2-Mg-ϵA-DNA complex), 5INK (mTdp2-Mg-THF complex), 5INL (mTdp2-Mg-dA-DNA-product complex), 5INM (mTdp2-apo structure), 5INN (mTdp2-D350N structure), 5INO (hTdp2-Mg-DNA product complex), 5INP (mTdp2-Mn-DNA product complex) and 5INQ (mTdp2-Ca-DNA product complex).

SUPPLEMENTARY DATA

Supplementary Data are available at NAR Online.

ACKNOWLEDGEMENTS

We thank L. Pedersen of the NIEHS Collaborative crystallography group for help with data collection. Data were collected at Southeast Regional Collaborative Access Team (SER-CAT) 22-ID beamline at the Advanced Photon Source, Argonne National Laboratory. We thank H. Wang and L. Pedersen for comments on the manuscript.

Author contributions: C.D.A. and B.M. performed mutagenesis expressed, purified and assayed mutant Tdp2 proteins. C.V. crystallized and solved the dA and ϵA-Tdp2 complexes. L.P. performed QM/MM analysis. M.S. crystallized Tdp2 and Tdp2-DNA complexes, solved crystal structures, synthesized modified oligonucleotide substrates and performed biochemical analyses. J.W. Performed mass spectrometry analysis of Tdp2 proteolysis fragments. D.R., C.S. and C.W. performed Tdp2 complementation assays and cellular NHEJ assays, and C.W. performed *in vitro* reactions and sequencing of cellular NHEJ products. R.S.W. managed the project. R.S.W., D.R., M.S. and L.P. wrote the manuscript with input from all authors.

FUNDING

US National Institute of Health Intramural Program; US National Institute of Environmental Health Sciences (NIEHS) [1Z01ES102765 to R.S.W.]; National Cancer Institute (NCI) [R01 CA084442 to D.A.R]. Use of the APS was supported by the U. S. Department of Energy, Office of Science, Office of Basic Energy Sciences, under Contract No. W-31-109-Eng-38. Funding for open access publication: NIEHS [1Z01ES102765 to R.S.W].

Conflict of interest statement. None declared.

REFERENCES

1. Nitiss,J.L. (2009) Targeting DNA topoisomerase II in cancer chemotherapy. *Nat. Rev. Cancer*, **9**, 338–350.
2. Nitiss,J.L. (2009) DNA topoisomerase II and its growing repertoire of biological functions. *Nat. Rev. Cancer*, **9**, 327–337.
3. Pommier,Y., Huang,S.Y., Gao,R., Das,B.B., Murai,J. and Marchand,C. (2014) Tyrosyl-DNA-phosphodiesterases (TDP1 and TDP2). *DNA Repair (Amst)*, **19**, 114–129.
4. Pommier,Y. (2013) Drugging topoisomerases: lessons and challenges. *ACS Chem. Biol.*, **8**, 82–95.
5. Andres,S.N., Schellenberg,M.J., Wallace,B.D., Tumbale,P. and Williams,R.S. (2015) Recognition and repair of chemically heterogeneous structures at DNA ends. *Environ. Mol. Mutagen.*, **56**, 1–21.
6. Wallace,B.D. and Williams,R.S. (2014) Ribonucleotide triggered DNA damage and RNA-DNA damage responses. *RNA Biol.*, **11**, 1340–1346.
7. Ashour,M.E., Atteya,R. and El-Khamisy,S.F. (2015) Topoisomerase-mediated chromosomal break repair: an emerging player in many games. *Nat. Rev. Cancer*, **15**, 137–151.
8. Gao,R., Schellenberg,M.J., Huang,S.Y., Abdelmalak,M., Marchand,C., Nitiss,K.C., Nitiss,J.L., Williams,R.S. and Pommier,Y. (2014) Proteolytic degradation of topoisomerase II (Top2) enables the processing of Top2.DNA and Top2.RNA covalent complexes by Tyrosyl-DNA-Phosphodiesterase 2 (TDP2). *J. Biol. Chem.*, **289**, 17960–17969.
9. Wang,Y., Knudsen,B.R., Bjergbaek,L., Westergaard,O. and Andersen,A.H. (1999) Stimulated activity of human topoisomerases IIalpha and IIbeta on RNA-containing substrates. *J. Biol. Chem.*, **274**, 22839–22846.
10. Wilstermann,A.M. and Osheroff,N. (2001) Base excision repair intermediates as topoisomerase II poisons. *J. Biol. Chem.*, **276**, 46290–46296.
11. Kingma,P.S., Corbett,A.H., Burcham,P.C., Marnett,L.J. and Osheroff,N. (1995) Abasic sites stimulate double-stranded DNA cleavage mediated by topoisomerase II. DNA lesions as endogenous topoisomerase II poisons. *J. Biol. Chem.*, **270**, 21441–21444.
12. Kingma,P.S. and Osheroff,N. (1997) Spontaneous DNA damage stimulates topoisomerase II-mediated DNA cleavage. *J. Biol. Chem.*, **272**, 7488–7493.
13. Kingma,P.S. and Osheroff,N. (1997) Apurinic sites are position-specific topoisomerase II poisons. *J. Biol. Chem.*, **272**, 1148–1155.
14. Kingma,P.S. and Osheroff,N. (1998) The response of eukaryotic topoisomerases to DNA damage. *Biochim. Biophys. Acta*, **1400**, 223–232.
15. Bolt,H.M. (2005) Vinyl chloride-a classical industrial toxicant of new interest. *Crit. Rev. Toxicol.*, **35**, 307–323.
16. Sabourin,M. and Osheroff,N. (2000) Sensitivity of human type II topoisomerases to DNA damage: stimulation of enzyme-mediated DNA cleavage by abasic, oxidized and alkylated lesions. *Nucleic Acids Res.*, **28**, 1947–1954.
17. Cortes Ledesma,F., El Khamisy,S.F., Zuma,M.C., Osborn,K. and Caldecott,K.W. (2009) A human 5'-tyrosyl DNA phosphodiesterase that repairs topoisomerase-mediated DNA damage. *Nature*, **461**, 674–678.
18. Gomez-Herreros,F., Schuurs-Hoeijmakers,J.H., McCormack,M., Greally,M.T., Rulten,S., Romero-Granados,R., Counihan,T.J., Chaila,E., Conroy,J., Ennis,S. *et al.* (2014) TDP2 protects

transcription from abortive topoisomerase activity and is required for normal neural function. *Nat. Genet.*, **46**, 516–521.

19. Gomez-Herreros,F., Romero-Granados,R., Zeng,Z., Alvarez-Quilon,A., Quintero,C., Ju,L., Umans,L., Vermeire,L., Huylebroeck,D., Caldecott,K.W. *et al.* (2013) TDP2-dependent non-homologous end-joining protects against topoisomerase II-induced DNA breaks and genome instability in cells and in vivo. *PLoS Genet.*, **9**, e1003226.
20. Schellenberg,M.J., Appel,C.D., Adhikari,S., Robertson,P.D., Ramsden,D.A. and Williams,R.S. (2012) Mechanism of repair of 5'-topoisomerase II-DNA adducts by mammalian tyrosyl-DNA phosphodiesterase 2. *Nat. Struct. Mol. Biol.*, **19**, 1363–1371.
21. Do,P.M., Varanasi,L., Fan,S., Li,C., Kubacka,I., Newman,V., Chauhan,K., Daniels,S.R., Boccetta,M., Garrett,M.R. *et al.* Mutant p53 cooperates with ETS2 to promote etoposide resistance. *Genes Dev.*, **26**, 830–845.
22. Otwinowski,Z. and Minor,W. (1997) In: Carter,CW Jr and Sweets,R.M. (eds). *Methods in Enzymology*. Academic Press, NY, Vol. **276**, pp. 307–326.
23. McCoy,A.J., Grosse-Kunstleve,R.W., Adams,P.D., Winn,M.D., Storoni,L.C. and Read,R.J. (2007) Phaser crystallographic software. *J. Appl. Crystallogr.*, **40**, 658–674.
24. Emsley,P., Lohkamp,B., Scott,W.G. and Cowtan,K. (2010) Features and development of Coot. *Acta Crystallogr. D Biol. Crystallogr.*, **66**, 486–501.
25. Adams,P.D., Afonine,P.V., Bunkoczi,G., Chen,V.B., Echols,N., Headd,J.J., Hung,L.W., Jain,S., Kapral,G.J., Grosse Kunstleve,R.W. *et al.* (2011) The Phenix software for automated determination of macromolecular structures. *Methods*, **55**, 94–106.
26. Davis,B.J., Havener,J.M. and Ramsden,D.A. (2008) End-bridging is required for pol mu to efficiently promote repair of noncomplementary ends by nonhomologous end joining. *Nucleic Acids Res.*, **36**, 3085–3094.
27. Waters,C.A., Strande,N.T., Pryor,J.M., Strom,C.N., Mieczkowski,P., Burkhalter,M.D., Oh,S., Qaqish,B.F., Moore,D.T., Hendrickson,E.A. *et al.* (2014) The fidelity of the ligation step determines how ends are resolved during nonhomologous end joining. *Nat. Commun.*, **5**, 4286.
28. Fattah,F., Lee,E.H., Weisensel,N., Wang,Y., Lichter,N. and Hendrickson,E.A. (2010) Ku regulates the non-homologous end joining pathway choice of DNA double-strand break repair in human somatic cells. *PLoS Genet.*, **6**, e1000855.
29. Yang,X., Boehm,J.S., Yang,X., Salehi-Ashtiani,K., Hao,T., Shen,Y., Lubonja,R., Thomas,S.R., Alkan,O., Bhimdi,T. *et al.* (2011) A public genome-scale lentiviral expression library of human ORFs. *Nat. Methods*, **8**, 659–661.
30. Frisch,M.J., Trucks,G.W., Schlegel,H.B., Scuseria,G.E., Robb,M.A., Cheeseman,J.R., Scalmani,G., Barone,V., Mennucci,B., Petersson,G.A. *et al.* (2009) Gaussian, Inc., Wallingford.
31. Batra,V.K., Perera,L., Lin,P., Shock,D.D., Beard,W.A., Pedersen,L.C., Pedersen,L.G. and Wilson,S.H. (2013) Amino acid substitution in the active site of DNA polymerase beta explains the energy barrier of the nucleotidyl transfer reaction. *J. Am. Chem. Soc.*, **135**, 8078–8088.
32. Bromberg,K.D., Hendricks,C., Burgin,A.B. and Osheroff,N. (2002) Human topoisomerase IIalpha possesses an intrinsic nucleic acid specificity for DNA ligation. Use of 5' covalently activated oligonucleotide substrates to study enzyme mechanism. *J. Biol. Chem.*, **277**, 31201–31206.
33. Woodfield,G., Cheng,C., Shuman,S. and Burgin,A.B. (2000) Vaccinia topoisomerase and Cre recombinase catalyze direct ligation of activated DNA substrates containing a 3'-para-nitrophenyl phosphate ester. *Nucleic Acids Res.*, **28**, 3323–3331.
34. Velez-Cruz,R., Riggins,J.N., Daniels,J.S., Cai,H., Guengerich,F.P., Marnett,L.J. and Osheroff,N. (2005) Exocyclic DNA lesions stimulate DNA cleavage mediated by human topoisomerase II alpha in vitro and in cultured cells. *Biochemistry*, **44**, 3972–3981.
35. Deweese,J.E. and Osheroff,N. (2009) The DNA cleavage reaction of topoisomerase II: wolf in sheep's clothing. *Nucleic Acids Res.*, **37**, 738–748.
36. Shi,K., Kurahashi,K., Gao,R., Tsutakawa,S.E., Tainer,J.A., Pommier,Y. and Aihara,H. (2012) Structural basis for recognition of 5'-phosphotyrosine adducts by Tdp2. *Nat. Struct. Mol. Biol.*, **19**, 1372–1377.
37. Gao,R., Huang,S.Y., Marchand,C. and Pommier,Y. (2012) Biochemical characterization of human tyrosyl-DNA phosphodiesterase 2 (TDP2/TTRAP): a Mg(2+)/Mn(2+)-dependent phosphodiesterase specific for the repair of topoisomerase cleavage complexes. *J. Biol. Chem.*, **287**, 30842–30852.
38. Dupureur,C.M. (2008) Roles of metal ions in nucleases. *Curr. Opin. Chem. Biol.*, **12**, 250–255.
39. Adhikari,S., Karmahapatra,S.K., Elias,H., Dhopeshwarkar,P., Williams,R.S., Byers,S., Uren,A. and Roy,R. (2011) Development of a novel assay for human tyrosyl DNA phosphodiesterase 2. *Anal. Biochem.*, **416**, 112–116.
40. Lowry,D.F., Hoyt,D.W., Khazi,F.A., Bagu,J., Lindsey,A.G. and Wilson,D.M. 3rd (2003) Investigation of the role of the histidine-aspartate pair in the human exonuclease III-like abasic endonuclease, Ape1. *J. Mol. Biol.*, **329**, 311–322.
41. Sherry,S.T., Ward,M.H., Kholodov,M., Baker,J., Phan,L., Smigielski,E.M. and Sirotkin,K. (2001) dbSNP: the NCBI database of genetic variation. *Nucleic Acids Res.*, **29**, 308–311.
42. Virgen-Slane,R., Rozovics,J.M., Fitzgerald,K.D., Ngo,T., Chou,W., van der Heden van Noort,G.J., Filippov,D.V., Gershon,P.D. and Semler,B.L. (2012) An RNA virus hijacks an incognito function of a DNA repair enzyme. *Proc. Natl. Acad. Sci. U.S.A.*, **109**, 14634–14639.
43. Koniger,C., Wingert,I., Marsmann,M., Rosler,C., Beck,J. and Nassal,M. (2014) Involvement of the host DNA-repair enzyme TDP2 in formation of the covalently closed circular DNA persistence reservoir of hepatitis B viruses. *Proc. Natl. Acad. Sci. U.S.A.*, **111**, E4244–E4253.
44. Freudenthal,B.D., Beard,W.A., Cuneo,M.J., Dyrkheeva,N.S. and Wilson,S.H. (2015) Capturing snapshots of APE1 processing DNA damage. *Nat. Struct. Mol. Biol.*, **22**, 924–931.
45. Hadi,M.Z., Ginalski,K., Nguyen,L.H. and Wilson,D.M. 3rd (2002) Determinants in nuclease specificity of Ape1 and Ape2, human homologues of Escherichia coli exonuclease III. *J. Mol. Biol.*, **316**, 853–866.